Journal of Fluids and Structures ▮ (▮▮▮▮) ▮▮▮–▮▮▮

Contents lists available at SciVerse ScienceDirect

Journal of Fluids and Structures

journal homepage: www.elsevier.com/locate/jfs

Vortex-induced vibrations of a diamond cross-section: Sensitivity to corner sharpness

Justin S. Leontini *, Mark C. Thompson

Fluids Laboratory for Aeronautical and Industrial Research (FLAIR), Department of Mechanical and Aerospace Engineering, Monash University, Melbourne, Victoria 3800, Australia

ARTICLE INFO

Article history:
Received 19 June 2012
Accepted 13 January 2013

Keywords:
Vortex-induced vibration
Fluid–structure interaction
Symmetry breaking

ABSTRACT

This paper studies the fluid–structure interaction of an elastically mounted square cross-section cylinder immersed in a free stream. The cross-section is mounted such that its sides are at 45° to the free stream direction, in a "diamond" configuration, and its motion is constrained to the transverse direction relative to the flow direction. Apart from the cross-section, this setup is the same as the majority of single-degree-of-freedom vortex-induced vibration studies of cylinders. Two-dimensional direct numerical simulations of this system have been performed. The Reynolds number based on the point-to-point distance of the cross-section has been fixed at Re=200). Simulations at this Reynolds number allow a direct comparison with previous results from circular cylinders, and therefore focus directly on the impact of the geometry.

The sensitivity of the flow, and therefore the motion of the cylinder, to geometrical effects is considered. This is done by rounding the two side corners (those pointing across the flow) at a given radius. For well-rounded corners, the flow behaviour resembles that of a circular cylinder undergoing vortex-induced vibration. However, below a critical radius, the dynamics are considerably altered. Highly disordered and irregular wakes and body motions are observed, as well as a synchronized, periodic P+S wake mode (Williamson and Roshko, 1988), which consists of a pair of vortices on one side, and a single vortex on the other side, shed per oscillation cycle, which results in a non-zero mean lift force. A period-doubled version of this P+S wake is also presented. The spatial structure, and the spatio-temporal symmetries of each of these modes is reported. The results show that even though the spatio-temporal symmetry of the flow is unaffected by the geometry when the body is rigidly mounted (the flow always saturating to a Kármán vortex street) geometric features such as sharp corners can induce a number of spontaneous symmetry breaking bifurcations when the body is elastically mounted. Which of these various modes is observed is shown to be a function of both the corner radius and the spring stiffness, expressed through the reduced velocity.

1. Introduction

Vortex-induced vibration (VIV) is a canonical problem of fluid–structure interaction. Bluff bodies that are long in one direction perpendicular to a freestream (such as a cylinder) are susceptible to this phenomenon. It is essentially a coupling

* Corresponding author. Tel.: +61 399051610.
E-mail address: Justin.Leontini@monash.edu (J.S. Leontini).

0889-9746/$ - see front matter © 2013 Elsevier Ltd. All rights reserved.
http://dx.doi.org/10.1016/j.jfluidstructs.2013.01.002

between the body motion, and the periodic shedding of vortices that occurs in the wake of such bodies, known as the von Kármán vortex street. If the body has some ability to elastically move or deform (which is true of nearly every practical structure, natural or engineered), there is the possibility of the periodic vortex shedding exciting a resonant frequency, resulting in large oscillations of the structure.

Typically, large oscillations occur in the cross-stream direction. Because of this, the classic experiment on VIV is that of a circular cylinder, elastically mounted, yet constrained to move only in the cross-stream direction, immersed in a free stream. This "classic" setup has been extensively researched, both experimentally and numerically. Many of the pertinent results can be found in a series of review papers (Bearman, 1984; Sarpkaya, 2004; Williamson and Govardhan, 2004). While these studies present results using a series of different parameters, there are only four independent parameters required to define the problem, assuming that the flow is incompressible and Newtonian, and the structure can be modeled as a damped linear oscillator. These are the Reynolds number $\mathrm{Re}=UD/\nu$, the mass ratio $m^*=m/m_\mathrm{f}$, the non-dimensional spring stiffness $k^*=kD^2/mU^2$ and the non-dimensional structural damping constant $c^*=cD/mU$. Here, U is the free stream velocity, D is the length scale of the body (the diameter for a circular cylinder), ν is the kinematic viscosity, m is the sprung mass of the body, $m_\mathrm{f}=\rho\pi D^2/4$ is the mass of fluid displaced by the body, where ρ is the fluid density, and k is the spring stiffness. For this paper, the geometry of the body can also be considered as a parameter, in this case characterized by the corner radius. This is, of course, only one way to modify the basic VIV problem. Others such as allowing the cylinder to oscillate in the transverse and streamwise direction (Lee et al., 2013), using a flexible cylinder (Bourguet et al., in press), or adding momentum to the boundary layer (Korkischko and Meneghini, 2012) have all recently been investigated.

Of interest to this study are the results for very low values of damping, and mass ratios $m^*=\mathcal{O}(1)$. The dynamics are a strong function of the spring stiffness, usually expressed through the non-dimensional reduced velocity, $U^*=U/f_\mathrm{n}D=1/\sqrt{(k^*)}$, where $f_\mathrm{n}=\sqrt{(k/m)}$ is the natural structural frequency. For Reynolds numbers $\mathrm{Re}=\mathcal{O}(10^4)$, a number of regimes have been identified for circular cylinders (Govardhan and Williamson, 2000; Khalak and Williamson, 1999). With increasing U^*, the first regime is the "initial branch", characterized by the oscillation amplitude rapidly increasing with increasing U^*, and where the response of the body and the wake are essentially periodic, at a frequency close to the vortex shedding frequency from a rigid cylinder. Further increasing U^* sees the onset of the "upper branch", characterized by large peak amplitude oscillations, at a frequency closer to the natural structural frequency. These oscillations also appear to be unstable, and essentially chaotic (Hover et al., 1998; Khalak and Williamson, 1999). In fact, the recent in-depth controlled oscillation experiments from Morse and Williamson (2010) have confirmed that purely periodic oscillations at the amplitude and frequency that characterize the upper branch are not stable. Further increasing U^* sees the onset of the "lower branch", characterized by large amplitude, synchronized oscillations of the body motion and vortex shedding, that appear periodic and very stable. The frequency of the oscillation is closer to the natural structural frequency (especially if the impact of a negative added mass is incorporated Govardhan and Williamson, 2000).

At lower Re, where the vortex shedding is laminar and purely two-dimensional (essentially $\mathrm{Re}\leq 200$), similar response regimes for circular cylinders have been identified. Blackburn and Henderson (1996) and Leontini et al. (2006a) have shown initial, chaotic, and periodic synchronized regimes exist for the low-Re case, indicating that the dynamics are similar in the two cases. One significant difference between the low- and high-Re cases, however, is the mode of vortex shedding associated with each regime. For the high-Re cases, variants of the "2P" wake mode, consisting of two pairs of vortices per oscillation cycle, are observed in the upper and lower branches. For the low-Re cases, "2S" wake modes are observed, consisting of two single vortices shed per oscillation cycle (similar to the classic Kármán vortex street shed from a rigid cylinder). The naming of these modes follows the nomenclature of the controlled oscillation study of Williamson and Roshko (1988). Govardhan and Williamson (2000) presented results that show that the 2P mode is formed by stretching and splitting of the forming vortex structures in the near wake. It appears that the strain in the near wake in the low-Re case is not enough to cause this split, hence the difference in wake mode.

Interestingly, in the related problem of a controlled transversely oscillating cylinder (where the body motion is decoupled from the flow, and externally controlled to be perfectly sinusoidal), the 2P mode still cannot be recovered for the low-Re, two-dimensional case. This is in spite of the use of very large amplitudes, that induce a large strain in the wake. Instead, an asymmetric "P+S" mode, consisting of a pair of vortices on one side, and a single vortex on the other side of the wake, is formed. This is an example of a spontaneous symmetry breaking bifurcation, where the spatio-temporal symmetry of the flow is different from that of the forcing. Leontini et al. (2006b) showed that in this externally controlled case, it was possible for this asymmetric mode to lead to positive energy transfer (from the fluid to the structure), indicating VIV can be supported by this mode. This result supports the VIV simulations of Singh and Mittal (2005), that showed VIV occurring with a P+S wake mode, but only at values of $\mathrm{Re}\simeq 300$, past the threshold where this wake mode is expected to become three-dimensional (Leontini et al., 2007). However, these results indicate that if the strain in the near wake is increased, these multi-vortex and asymmetric wake modes resulting from spontaneous symmetry breaking can be encountered. As the results of this paper attest, this can occur through changes to the geometry as well as changes to Re.

This last point, i.e., the influence of the geometry of the oscillating body, is one that has received little attention with regard to VIV. Bearman et al. (1987) performed wind-tunnel experiments of an elastically mounted square-section cylinder, investigating the VIV response, as well as the galloping response at high values of U^*. Bokaian and Geoola (1984) did similar experiments, including experiments using square-section cylinders with rounded corners. These results indicated that the largest responses were due to galloping (a fluid–elastic instability). However, VIV was present, and the

Please cite this article as: Leontini, J.S., Thompson, M.C., Vortex-induced vibrations of a diamond cross-section: Sensitivity to corner sharpness. Journal of Fluids and Structures (2013), http://dx.doi.org/10.1016/j.jfluidstructs.2013.01.002

amplitude and frequency of response was found to be quite sensitive to the corner radius of the rounded-corner square section. Recently, water channel experiments of a square cross-section at varying angles of attack were performed by Zhao et al. (2010) and Nemes et al. (2012). These reported similar VIV results for the square cross-section at 45° (essentially a diamond cross-section) as for the circular cylinder. However, high-amplitude VIV-type responses, at frequencies half that of regular VIV, were reported for angles around 20°.

A numerical study from Sánchez-Sanz and Velazquez (2009) of a free-floating (with no restoring spring force) square-section cylinder in a confined channel identified two regimes of response as a function of the mass ratio m^*, one essentially periodic (for high m^*), and another essentially chaotic (for low m^*). This case is intriguing, as it can be interpreted as being at $U^* \to \infty$. The highly successful theory of galloping from Parkinson and Smith (1964) predicts that such a case should oscillate with unbounded amplitude (which could practically manifest as a persistent cross-stream drift in one direction); however, the effect of the channel walls in the simulations of Sánchez-Sanz and Velazquez (2009) works to limit this amplitude, in both the high- and low-m^* regimes.

More common than VIV studies are externally controlled oscillation studies of non-circular bodies. For example, Deniz and Staubli (1997) performed controlled oscillation experiments of rectangular- and octagonal-section cylinders. This study highlighted the importance of timing of the vortex shedding from the trailing edge of these structures to the direction of energy transfer (energy transfer must be from fluid to structure for VIV to be possible). A recent paper from Ajith Kumar et al. (2009), which included a thorough literature review, looked specifically at the effect on the flow of rounding the corners of a square cylinder undergoing controlled oscillations. They found that sharper corners led to disordered vortex shedding, essentially destroying the synchronization between the oscillation and vortex shedding.

A number of other studies do exist that investigate the impact of corner geometry and other geometrical modifications on rectangular section cylinders, both rigidly mounted and oscillating. Tamura et al. (1998), in a combined numerical and experimental study, found either rounding or chamfering the corners of a square-section cylinder led to a significant decrease in the drag on the rigidly fixed body. A similar conclusion was drawn from the numerical study of Dalton (2003), for both a square section and a square section at 45°, in a "diamond" configuration. Sheard et al. (2009) looked at squares of various angles of incidence, and found that for the sharp corner diamond case, a symmetry-breaking bifurcation arose, that could be suppressed simply by rounding the rear corner of the body. This result in particular indicates that even completely passive geometrical features, that do not modify the symmetry of the system (which includes the geometry and the domain boundary conditions), can have an impact on the symmetry features of the flow. The controlled oscillation experiments of Deniz and Staubli (1997) highlighted the impact that corner geometry could have by changing the length of the afterbody (the body downstream of the separation points of the shear layers), especially on the lift force experienced by the body, a critical parameter in the excitation of VIV. They also highlighted the importance of identifying whether the vortex shedding occurred from the leading or trailing edges of the body, a feature that is completely removed when considering a circular cylinder.

The apparently destabilizing nature of sharp corners makes it difficult to derive phenomenological models of VIV for these bodies. Typically, these models rely on measuring aerodynamic forces during controlled oscillations, such as the model from Hartlen and Currie (1970), and that from Staubli (1983). Corless and Parkinson (1988) had some success applying the model from Hartlen and Currie (1970) to square section cylinder VIV, after combining it with the model for galloping developed by Parkinson and Smith (1964). This was later extended and improved by Corless and Parkinson (1993). However, developing such a model is a formidable task, due not only to the coupling between pure VIV features and fluid–elastic galloping, but also to the fluctuating, and at times chaotic, flow that can occur from controlled oscillations, which make the reliable measurement of aerodynamic forces very difficult.

This paper shows that the sharpness of the side corners of a diamond (those from which the forming shear layers separate) has a major impact on the oscillation amplitude, induced forces, and temporal character of the elastically mounted system. A study of fixed bodies, with various corner radii is presented in Section 2.3, which shows that while the magnitude of lift and drag forces can be influenced by the corner sharpness, the flow remains periodic. However, the results for the elastically mounted cylinder, presented in Section 3, show that the corner sharpness can completely change the type of flow response. Seven modes of shedding and cylinder response are identified. Each of these modes is characterized by its temporal behaviour and wake mode, which are outlined. The extent of each of these modes, in terms of corner radius r_c and reduced velocity U^* is also presented.

2. Methodology and problem setup

2.1. Equations of motion, system parameters and computational method

The problem studied was that of a body, of mass m, mounted on linear springs of stiffness k, immersed in a free stream of a viscous incompressible fluid. The body was constrained to oscillate only in the cross-stream direction. As such, the flow was governed by the incompressible Navier–Stokes equations, and the body motion by the equation of motion for a linear oscillator. To account for the body motion, the Navier–Stokes equations were solved in the frame of reference attached to the body, and an extra term was added to account for the acceleration of this frame (which was the acceleration of the body, $\ddot{y}$). This method avoids the need for any mesh deformation, resulting in a computation with

Please cite this article as: Leontini, J.S., Thompson, M.C., Vortex-induced vibrations of a diamond cross-section: Sensitivity to corner sharpness. Journal of Fluids and Structures (2013), http://dx.doi.org/10.1016/j.jfluidstructs.2013.01.002

consistent spatial resolution over time. The final non-dimensional system of equations to be solved was

$$\frac{\partial \mathbf{u}}{\partial \tau} = -(\mathbf{u}\cdot\nabla)\mathbf{u} - \nabla P + \frac{1}{\mathrm{Re}}\nabla^2\mathbf{u} - \ddot{y},$$
$$\ddot{y} = -k^* y + \frac{1}{m^*}\mathrm{C_l}, \tag{1}$$

where $\mathrm{C_l} = F_l/0.5\rho U^2 D$ is the lift coefficient for the two-dimensional flow. Here, D is the point-to-point distance of the body. This choice of the length scale D is further explained in Section 2.2.

Note that no mechanical damping is included in the equations of motion. The Reynolds number was held constant at $\mathrm{Re}=200$, and the mass ratio was set to $m^*=2$ for all of the simulations conducted. This value of m^* was chosen so that the body would be light and therefore expected to oscillate with significant amplitude, but not so light as to be near any critical mass (Govardhan and Williamson, 2002; Ryan et al., 2005), below which the dynamics may not be generic. The value of Re was chosen to be in the vicinity of the upper limit for two-dimensional flow for a circular cylinder. The Floquet stability analysis of Sheard et al. (2009) indicates that the wake of the sharp corner diamond becomes three-dimensional at lower Re than this. However, it is expected that the transverse oscillation will be stabilizing with regard to three-dimensional perturbations, and keeping Re constant at this value allows the focus of this study to remain on the impact of the geometry only.

The system parameter that has been varied was that of the spring stiffness, k^*. However, following the convention of other VIV studies, the stiffness has been expressed through the reduced velocity, U^*. Previous studies of VIV of circular cylinders (Govardhan and Williamson, 2000; Khalak and Williamson, 1999) have "corrected" the reduced velocity by including an added mass term in the calculation of the natural frequency, to account for the inertia of the fluid that needs to be moved, derived from the inviscid added mass. However, for non-circular bodies, it is not obvious that the inviscid added mass will be as applicable due to the variation in the effective angle of attack of the body as it oscillates. Therefore, U^* has been formed without this added mass correction.

The equations have been solved using a spectral-element method, employing seventh-order tensor-product Lagrange polynomials as shape functions for the spatial discretization. Temporal discretization has been done via a three-way time-splitting scheme. This scheme results in separate sub-step equations for the advection and body acceleration terms, the pressure term, and the diffusion term. Further, by enforcing continuity at the end of the pressure sub-step, a Poisson equation is formed that can be solved for the pressure field. The advection sub-step equation was solved using a second-order semi-implicit predictor–corrector method, whereas the diffusion sub-step equation was solved using a second-order Crank–Nicholson scheme. Details of the spectral-element and time-splitting schemes can be found in Karniadakis and Sherwin (2005). This code has been used and extensively validated for similar problems, such as three-dimensional cylinder flows (Thompson et al., 1996), controlled transverse-, rotational- and streamwise-oscillating cylinder wakes (Leontini et al., 2006b; Lo Jacono et al., 2010; Leontini et al., 2011), and cylinder VIV studies (Leontini et al., 2006a).

The boundary conditions applied in the accelerating frame of reference were a no-slip condition at the body surface, a free stream condition at the inlet and sides of the domain (a constant streamwise component with a transverse component equal to the negative of the body velocity), and a Neumann boundary condition for the velocity, with fixed pressure, applied at the domain outflow. A Neumann boundary condition, with the value of the normal gradient calculated directly from the Navier–Stokes equations, was used for the pressure at the body surface and free stream domain boundaries. The domain extended $7.07D$ upstream, $18.38D$ to either side, and $28.99D$ downstream of the body centre position. All simulations used an initial condition of the flow and body at rest, with the flow impulsively started.

2.2. Geometry and choice of length scale

The nominal geometry tested was that of a square cross-section, inclined at 45° to the incoming flow, in a "diamond" configuration. This configuration presents two possible length scales; the side length of the square, or the distance from point-to-point, which is the frontal width seen by the flow. For all the results presented here, the length scale, D, is the point-to-point distance (for Re and U^*). Note that the square side length is simply $D/\sqrt{2}$.

Formally, D has been defined as the distance from front to back of the diamond. This is due to the fact that the side corners have been progressively rounded, to investigate the impact of fixing the separation points of the developing shear layers. Therefore, a geometric parameter, the corner radius, has been introduced. Throughout this paper, the corner radius is presented as a percentage of the side length, rather than the point-to-point distance, $r_c = \sqrt{2}r/D$, where r is the corner radius. Using this definition, $r_c = 0$ represents the limiting sharp corner case, and $r_c = 0.5$ represents the case where the foci of each of the curved corners is the exact centre of the cross-section. Values in the range $0 \le r_c \le 0.2$ have been tested. The definition of D and r_c are shown schematically in Fig. 1.

2.3. Validation and fixed body simulations

This section presents results from a series of simulations for the rigidly mounted, non-oscillating case, to assess the impact of rounding the corners of the geometry on this limiting case. As mentioned in Section 2.1, the code employed has been extensively validated in previous studies of bluff body flows, including vortex-induced vibration. However, due to the

Please cite this article as: Leontini, J.S., Thompson, M.C., Vortex-induced vibrations of a diamond cross-section: Sensitivity to corner sharpness. Journal of Fluids and Structures (2013), http://dx.doi.org/10.1016/j.jfluidstructs.2013.01.002

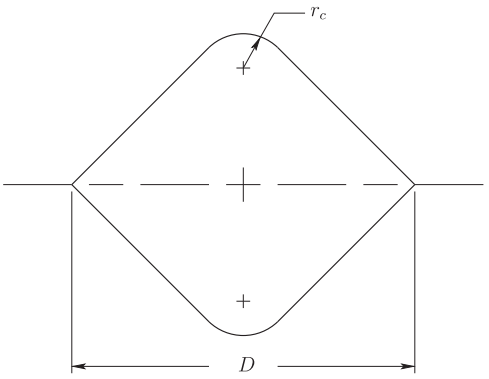

Fig. 1. The geometry of the body tested. The corner radius $r_c = \sqrt{2}r/D$ (the radius as a fraction of side length) varies from $r_c = 0$ (the sharp corner limiting case) to $r_c = 0.2$. D is defined as the distance from the front to back corner.

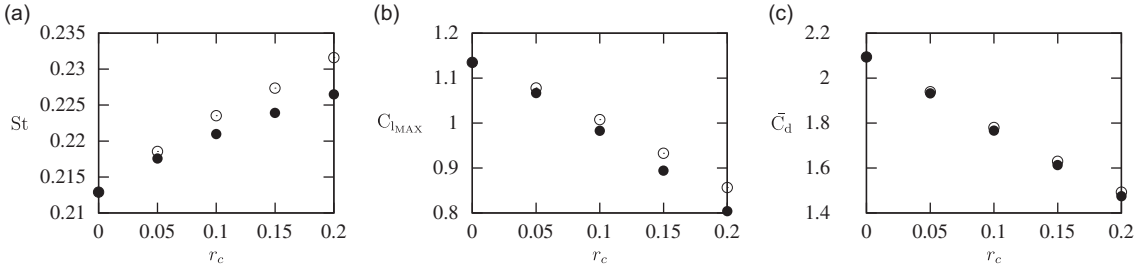

Fig. 2. (a) Strouhal number, (b) peak lift coefficient, and (c) mean drag coefficient, all as functions of the corner radius r_c. Open circles (○) represent results for $\mathrm{Re}_{\mathrm{trans}} = 200$, black circles represent results for $\mathrm{Re} = 200$. These results show that, over the range of r_c tested, the value of the corner radius has a larger impact than the change in $\mathrm{Re}_{\mathrm{trans}}$ if Re is held constant.

small geometric length scales involved in this study (especially for finite, but small corner radii), a resolution test has been carried out to ensure the accuracy of the results.

2.3.1. *Fixed body simulations*

As a primary aim of this paper is to establish the impact of the sharp corners, simulations of rounded corner, rigidly mounted bodies have been performed. The quantities of these simulations that are reported here are those most pertinent to vortex-induced vibration, namely the Strouhal number, and the peak lift force coefficient. For completeness, the mean drag coefficient is also reported.

Two sets of simulations have been performed; one set with a Reynolds number based on D, the streamwise length as shown in Fig. 1, fixed at $\mathrm{Re}=200$ and a second set with $\mathrm{Re}_{\mathrm{trans}} = 200$, based on the cross-stream length, where $\mathrm{Re}_{\mathrm{trans}} = U(D - r_c(2\sqrt{2}-1))/\nu$. Therefore, for this second set of simulations, Re increases linearly with r_c. For the largest corner radius of this study, $r_c = 0.20$, $\mathrm{Re}=226.5$ when $\mathrm{Re}_{\mathrm{trans}} = 200$.

Fig. 2 shows the results for both these sets of simulations. For all of these fixed body simulations, the flow settled to a purely periodic, classic von Kármán vortex street. The Strouhal number representing the frequency of this vortex street is shown in Fig. 2a. It is shown to be weakly dependent on the corner radius. Some Reynolds number dependence is shown by the difference between the two sets of simulations. However, at $r_c = 0.20$, where the difference in Re for the two sets is larger than 10%, the difference in Strouhal number is less than 2.5%. The peak lift coefficient shows a similar behaviour in Fig. 2b, in that the Reynolds number dependence is relatively weak. However, the dependence on r_c is reasonably strong, confirming that the sharp corners have a significant impact on the shear layer separation and wake vortex formation. For similar reasons, the mean drag is shown in Fig. 2c to be strongly dependent on the r_c, while only weakly dependent on Re.

These results validate the choice to keep Re constant, based on the point-to-point distance D, as it seems the geometric parameter r_c has a larger impact than any "error" induced by a varying length scale. Also, the smooth variation of all the parameters plotted in Fig. 2 gives a high degree of confidence in the results at small corner radii, indicating that the simulations are adequately resolved to capture the effect of the small geometrical change. A more complete resolution study is presented in Section 2.3.2.

2.3.2. *Resolution tests for small corner radii*

The body motion, especially for the bodies with small corner radii, can be very complex, even chaotic as is described in Section 3.3. For this reason, it is important to establish that this complex motion is due to the geometrical effect of the

Please cite this article as: Leontini, J.S., Thompson, M.C., Vortex-induced vibrations of a diamond cross-section: Sensitivity to corner sharpness. Journal of Fluids and Structures (2013), http://dx.doi.org/10.1016/j.jfluidstructs.2013.01.002

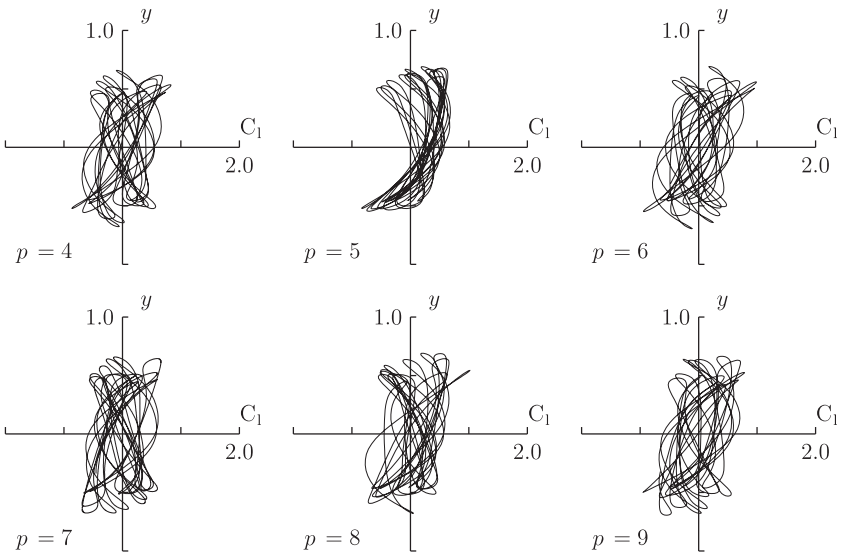

Fig. 3. Lissajou plots, of lift against displacement, for six different spatial resolutions, with resolution increasing from left to right, top to bottom. The data are from a simulation with $r_c = 0.01$, $U^* = 4.95$. The plots show that the response is qualitatively similar for $p > 6$.

Table 1
Maximum body displacement, y_p, maximum lift coefficient, $C_{l_{MAX}}$, and maximum drag coefficient, $C_{d_{MAX}}$, as functions of the order of the polynomial shape functions, p, from a simulation for a body of $r_c = 0.01$ and $U^* = 4.95$. These peak values vary little with the change in polynomial order, indicating that $p=7$ is adequate to capture the physics of the problem.

p	y_p	$C_{l_{MAX}}$	$C_{d_{MAX}}$
4	0.68599	0.86168	4.08687
5	0.70205	1.02799	4.14989
6	0.70534	1.02140	4.15620
7	0.69378	1.01586	4.16968
8	0.69383	1.01498	4.14920
9	0.70539	0.94421	4.11450

sharp corner, and not some residual effect of under-resolution. Therefore, a resolution test for a case with $r_c = 0.01$, and $U^* = 4.95$, has been carried out.

Fig. 3 shows Lissajou plots, of lift coefficient against body displacement, for six different spatial resolutions. To vary the spatial resolution, the macro-element mesh was kept the same, and the order of the polynomial shape functions was increased, a process known as p-refinement. The plots show that for $p > 6$, the responses are qualitatively similar, covering a bounded region in the Lissajou plot, but never quite repeating, indicative of a chaotic response. These plots also show that, for $p > 6$, there is a quantitative agreement between the peak lift and displacement values.

Table 1 shows values of peak body displacement, lift and drag coefficients for the same simulations. The table shows that the changes in these peak quantities with a change in polynomial order are relatively minor, typically less than 1% compared with the results at $p=7$.

These results indicate that the simulations are adequately resolved at $p=7$, and it is this resolution that has been used for the simulations that have generated the results of the current study.

3. Elastically mounted simulations

3.1. Peak amplitudes

The traditional measure of VIV response has been the peak amplitude of oscillation. There are two primary reasons for this. The first is the importance in engineering applications to identify the deflections, and therefore stresses, encountered by a structure undergoing VIV. The second is that the traditional model of VIV has been of a lightly damped harmonic oscillator (the body) undergoing a periodic forcing from the vortex shedding. This model admits only harmonic body oscillations, meaning that only the peak amplitude and frequency of oscillation are required to completely describe the motion.

This simple model ignores the coupling between the body motion and the flow. This is not a problem during fully synchronized VIV, such as occurs during "lower branch" oscillations, or during VIV of very light structures (Govardhan and

Please cite this article as: Leontini, J.S., Thompson, M.C., Vortex-induced vibrations of a diamond cross-section: Sensitivity to corner sharpness. Journal of Fluids and Structures (2013), http://dx.doi.org/10.1016/j.jfluidstructs.2013.01.002

Williamson, 2000, 2002). During these synchronized motions, the motion and the transverse fluid force is almost purely sinusoidal, and the assumptions made in the model are valid. However, the picture is not as clear when the flow is not completely synchronized to the body motion. Typical "upper branch" oscillations occur with the flow intermittently switching between two apparently periodic states, neither of which are stable. Hover et al. (1998) reported chaotic oscillations at values of U^* corresponding to the upper branch. Leontini et al. (2006a) and Blackburn and Henderson (1996) have also reported chaotic oscillations during VIV from two-dimensional simulations for $\mathrm{Re} < 200$.

Fig. 4a presents a measure of the peak amplitude of oscillation for all of the geometries considered. Also presented on the plot is the peak amplitude of oscillation of a circular cylinder at the same Re and m^*. The data presented is the maximum deviation from the mean position of the body. For symmetric oscillations about $y=0$, this is the same as the peak amplitude, and provides a more meaningful measure of magnitude for asymmetric oscillations. Fig. 4b presents the absolute value of the mean body position. This gives a direct indication of when the body oscillates asymmetrically.

There are a number of features of Fig. 4 that warrant some explanation. It is clear that the magnitude and symmetry of the oscillations is a function of both the corner radius and U^*.

In one sense, the trend of maximum deviation with U^* is similar to that of a circular cylinder. For very low U^*, there is essentially no response. Then over a range of U^* beginning with $U^* \simeq 3.5$, there is a significant oscillation amplitude. In the case of a circular cylinder, this significant response is driven by a synchronization between the body oscillation and vortex shedding frequencies, and occurs when the natural frequency of the structure is in the vicinity of the vortex shedding frequency from a stationary body. As expected, it appears that similar dynamics occur for the non-circular geometries.

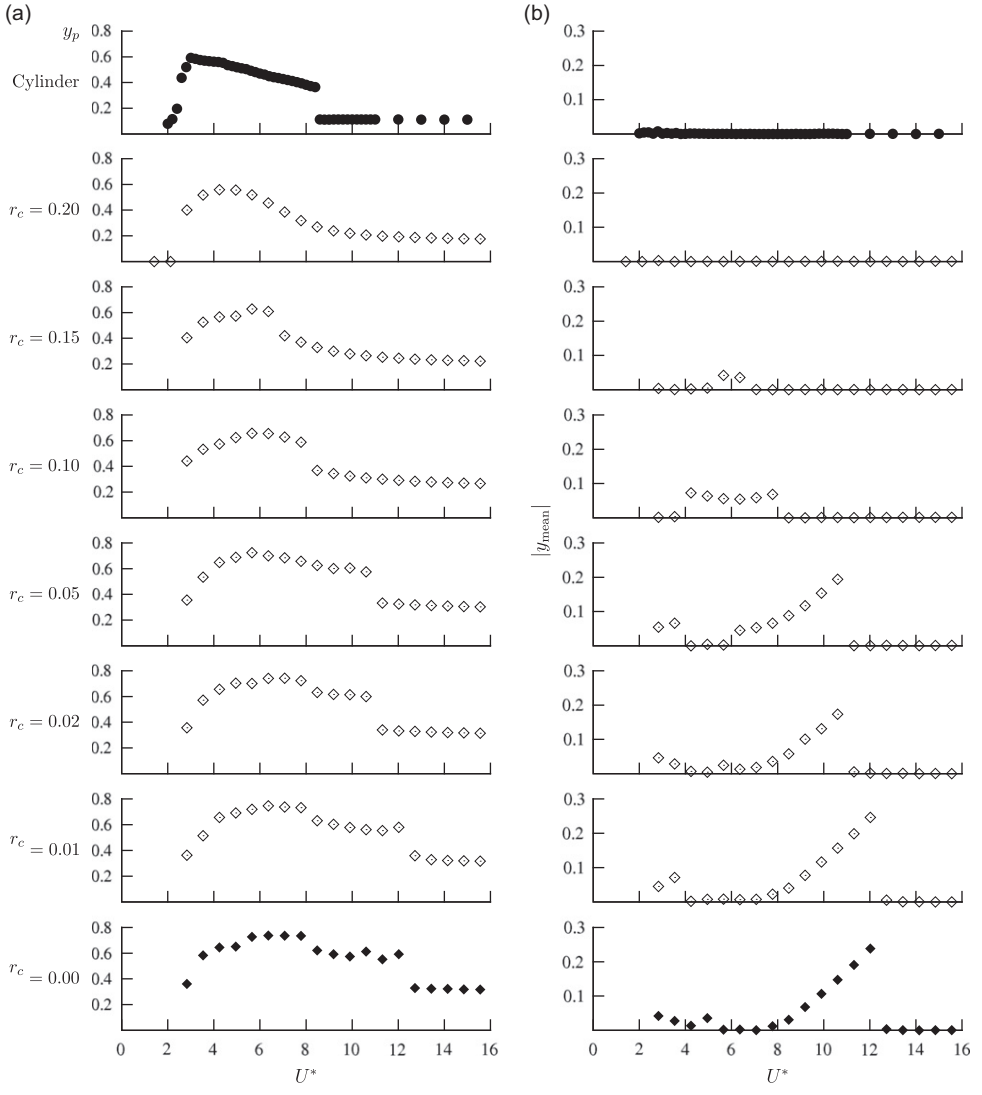

Fig. 4. (a) Maximum deviation from the mean body position as a function of U^*, for all the corner radii and a circular cylinder. Cylinder data is presented in the top graph (•), with diamond geometries of decreasing corner radius presented below (◇), finishing with the sharp corner case (◆). (b) The mean body position for the same bodies as a function of U^*.

Please cite this article as: Leontini, J.S., Thompson, M.C., Vortex-induced vibrations of a diamond cross-section: Sensitivity to corner sharpness. Journal of Fluids and Structures (2013), http://dx.doi.org/10.1016/j.jfluidstructs.2013.01.002

For $U^* > 12.5$, the response amplitude decreases again, as the resonance-type effect between the vortex shedding and natural structural frequencies is lost. Three broad response regimes can therefore be defined from the data of Fig. 4a: a low-U^* regime, where the body remains essentially stationary; a moderate-U^* regime, where there is significant body motion; and a high-U^* regime, where the body oscillates with a lower, but still significant amplitude. In this high-U^* regime, the amplitude of oscillation approaches a constant value with increasing U^* that is an inverse function of r_c.

Of particular interest is the behaviour in the moderate-U^* regime. The peak amplitude and mean body displacement, in this regime, are strong functions of r_c. Fig. 4 indicates that there is a number of unique response types within this regime. The nature of these difference responses is explained in Sections 3.3 and 3.4.

3.2. Frequency spectra

The variation of the peak amplitude and the mean body displacement with U^*, particularly for the bodies with $r_c \leq 0.05$, indicates that the peak amplitude does not fully characterize the response, and other information is required. Of interest is the frequency response of the system. For this reason, frequency spectra covering a range of U^* and r_c are presented in this section.

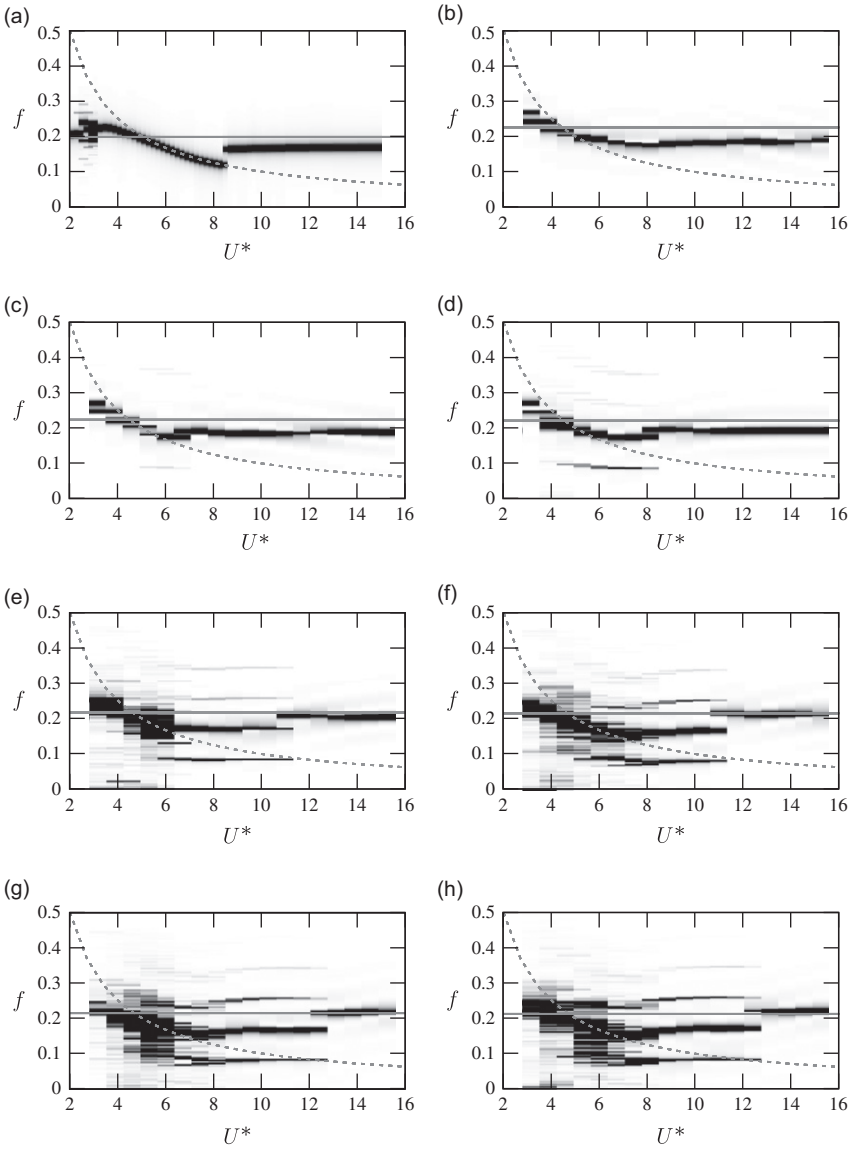

Fig. 5. Frequency content as a function of U^* for (a) the circular cylinder, and for the diamond geometries with decreasing corner radii of (b) 0.20, (c) 0.15, (d) 0.10, (e) 0.05, (f) 0.02, (g) 0.01, (h) 0.0 (the sharp corner case). The dashed line represents the natural frequency, f_n, the solid horizontal line represents the Strouhal frequency for the rigidly mounted body. The chaotic regime is represented by broadband noise, normal periodic shedding by a single concentrated value, and the abnormal periodic regime by distinct, but multiple frequencies. With decreasing radius, the emergence of first the abnormal periodic regime, and then the chaotic regime, is clear.

Please cite this article as: Leontini, J.S., Thompson, M.C., Vortex-induced vibrations of a diamond cross-section: Sensitivity to corner sharpness. Journal of Fluids and Structures (2013), http://dx.doi.org/10.1016/j.jfluidstructs.2013.01.002

Each plot of Fig. 5 shows the frequency content (where frequency has been non-dimensionalized by D/U) of the body oscillation for a given value of r_c, as a function of U^*. These plots were constructed by taking the frequency spectrum (using a Fourier transform) for a given value of U^*, and then stacking the spectra for all the values of U^* next to each other. To make the dominant frequencies clearly visible, each individual spectrum (for a single value of U^*) was normalized by the amplitude of the dominant component, so that the levels varied from 0 to 1. While this means that the level at a particular frequency as a function of U^* cannot be ascertained directly, a very clear picture of the variation of the dominant frequencies is presented.

Fig. 5a shows the progression of the frequency content of the body oscillation for a circular cylinder. there is a small band, $3.0 \leq U^* \leq 3.3$, which corresponds to chaotic oscillations. This is represented in Fig. 5a as the dark region in the frequency range $0.17 \leq f \leq 0.22$, the chaotic oscillations requiring this band of frequencies for their description. This small band of chaotic oscillation is important as it is within this band that the highest peak oscillations occur. With the onset of synchronized periodic shedding at $U^* = 3.3$, this broadband character disappears, and only a single frequency component remains. In this synchronized regime, the frequency of oscillation approaches a frequency similar to the natural structural frequency of the body with increasing U^*. Finally, when synchronization is lost for $U^* > 8.4$, the response is dominated by a single frequency close to the Strouhal frequency (the frequency of vortex shedding from a fixed cylinder).

The picture is similar for the frequency response of the diamond geometry with the most rounded corners, $r_c = 0.20$, presented in Fig. 5b. Again, the onset of significant amplitude oscillations, around $U^* = 3.5$, sees the frequency response dominated by a single frequency somewhere near the natural structural frequency. This continues until $U^* \simeq 7.0$. From thereon, the single frequency of response stays close to the Strouhal frequency for the fixed body.

Fig. 5c and d shows the frequency response for the bodies with $r_c = 0.15$ and $r_c = 0.10$, respectively. These plots are similar to the case at $r_c = 0.20$, except for one important difference; the addition of significant energy at a frequency half of the primary frequency over a small band of U^* near $U^* = 5.6$. This is particularly clear for the $r_c = 0.10$ case, over the range $5.6 \leq U^* \leq 7.8$. This range coincides with that where the mean body position $u_{\text{mean}} \neq 0$, in Fig. 4b. The combined observations indicate that the oscillation in this range is periodic, but over a period close to half of the natural structural frequency, as well as being asymmetric.

Further reduction of the corner radius to $r_c = 0.05$ sees the frequency response become even more complicated, represented in Fig. 5e. As well as an extended asymmetric shedding range, the frequency response over the range $2.8 \leq U^* \leq 6.4$ is more broadband, indicating the onset of chaotic, or at least temporally complex, oscillations.

In fact, for corner radius $r_c \to 0$, this appears to be the general case. With increasing U^*, first a regime of temporally complex oscillations exists, followed by a regime of periodic, yet asymmetric oscillations, finally followed by a regime of smaller amplitude, yet apparently periodic oscillations, at a frequency close to the Strouhal frequency of the fixed body. Fig. 5f, g, h, shows this behaviour reflected in the frequency response for corner radii $r_c = 0.02$, $r_c = 0.01$, and the limiting sharp-corner case $r_c = 0.00$, respectively. These plots show that as the corner radius is decreased, the range of U^* over which the temporally complex oscillations exist extends. Similar to the circular cylinder, comparison of the frequency response plots with Fig. 4a shows that the largest peak oscillation amplitudes are achieved in this complex oscillation regime.

Combining the information presented in Figs. 4 and 5 leads to defining three broad categories of response, as a function of the corner radius, r_c. First, for large corner radii, approximately $r_c > 0.15$, the flow response is similar to that of the circular cylinder. This cylinder-like response is perhaps not surprising, as the rounded corners do not fix the separation points of the shear layers, and therefore the vortex formation process is not markedly different from that of a circular cylinder, in spite of the sharp leading and trailing edges.

At the other extreme, for the limiting case $r_c = 0$, the response is markedly different. This "diamond-like" response has significant ranges of U^* resulting in temporally complex and asymmetric shedding. Due to the fact that these complex oscillations also lead to the largest peak amplitudes of oscillation, they warrant closer inspection, and are therefore the subject of Section 3.3.

Between these two extremes, the response varies from "diamond-like" to "cylinder-like". With increasing r_c, the ranges of U^* for the temporally complex oscillations, and the asymmetric oscillations, reduce. The complex oscillations appear to completely disappear at a smaller value of r_c than the asymmetric oscillations.

3.3. *Further investigation of the temporally complex oscillations and flow regimes of the sharp corner case*

The information presented in Figs. 4 and 5 indicate that a number of flow regimes exist. The spectra of Fig. 5 show that for small corner radii (including the limiting sharp-corner case $r_c = 0.0$), there is a region of temporally complex oscillations that encompass the range of U^* where the largest peak oscillations occur. In fact, this region encompasses a series of flow subregimes, which are expanded upon in this section. The sharp corner case appears to generate almost all of the flow regimes observed, and so it is used as an example case wherever possible in this section, allowing the flow regimes observed to be presented as a function of U^*.

For very low U^*, the flow is essentially periodic, with a frequency close to the Strouhal frequency for the fixed body. This is to be expected, for as $U^* \to 0$, the spring stiffness $k^* \to \infty$, and the system approaches the rigid case. The vortex shedding is in the classic von Kármán mode, or a 2S configuration, consisting of a single vortex on each side of the wake in each cycle. This regime is therefore designated mode I.

Please cite this article as: Leontini, J.S., Thompson, M.C., Vortex-induced vibrations of a diamond cross-section: Sensitivity to corner sharpness. Journal of Fluids and Structures (2013), http://dx.doi.org/10.1016/j.jfluidstructs.2013.01.002

By $U^* = 2.8$, the flow has gone through a symmetry-breaking bifurcation, as evidenced by the non-zero mean displacement shown in Fig. 4b. This symmetry breaking can correspond to a change in shedding mode, to a P+S type mode, consisting of a pair of vortices on one side of the wake, and a single vortex on the other, each cycle of oscillation, or even modes that are essentially asymmetric 2P modes, consisting of two pairs of vortices per cycle. This mode has been designated mode II.

Increasing U^* beyond $U^* = 3.1$ sees this mode II become unstable, and the onset of temporally complex oscillations. A number of subregimes are present in this regime, and to further investigate this region, Lissajou plots of the body displacement against the lift force on the body have been produced. Examples of these plots for the sharp-corner case $r_c = 0.0$ are shown in Fig. 6 for simulations covering the range $2.8 \leq U^* \leq 8.5$. To accompany these plots, the individual frequency spectra for these simulations are presented in Fig. 7. These plots contain the same information as that used to produce Fig. 5b, but give a finer-scale picture of the variation of the frequency content in the complex oscillation regime.

Fig. 6a shows the Lissajou plot for $U^* = 2.8$, just before the onset of complex oscillations. The closed curve, that is slightly offset from the centre of the plot, is indicative of the periodic, but asymmetric nature of mode II. The frequency spectrum for this case in Fig. 7a shows that almost all of the energy is contained in the component at the primary frequency of oscillation (except for a small component at three times the primary frequency, a common occurrence during VIV).

The loss of stability of mode II sees this periodicity disappear. For $U^* = 3.5$, the curve traced out in the Lissajou plot of Fig. 6b is more disordered, but not completely chaotic. Rather the flow is close to periodic, with a slight drift, or essentially quasiperiodic. The frequency spectrum of the motion shown in Fig. 7b is noisier than the purely periodic case, but most of the energy is still concentrated in the primary frequency of oscillation. This is not the classic signature of quasiperiodicity (which would be a series of well-defined peaks), but shows that the flow is not "very" disordered, in some sense. This mode has been designated mode III.

Further increasing U^* to $U^* = 4.2$ sees the level of disorder increase, and the trace in the Lissajou plot of Fig. 6c follows a highly irregular trajectory. This, coupled with the increasingly broadband signature of the frequency spectrum of Fig. 7c,

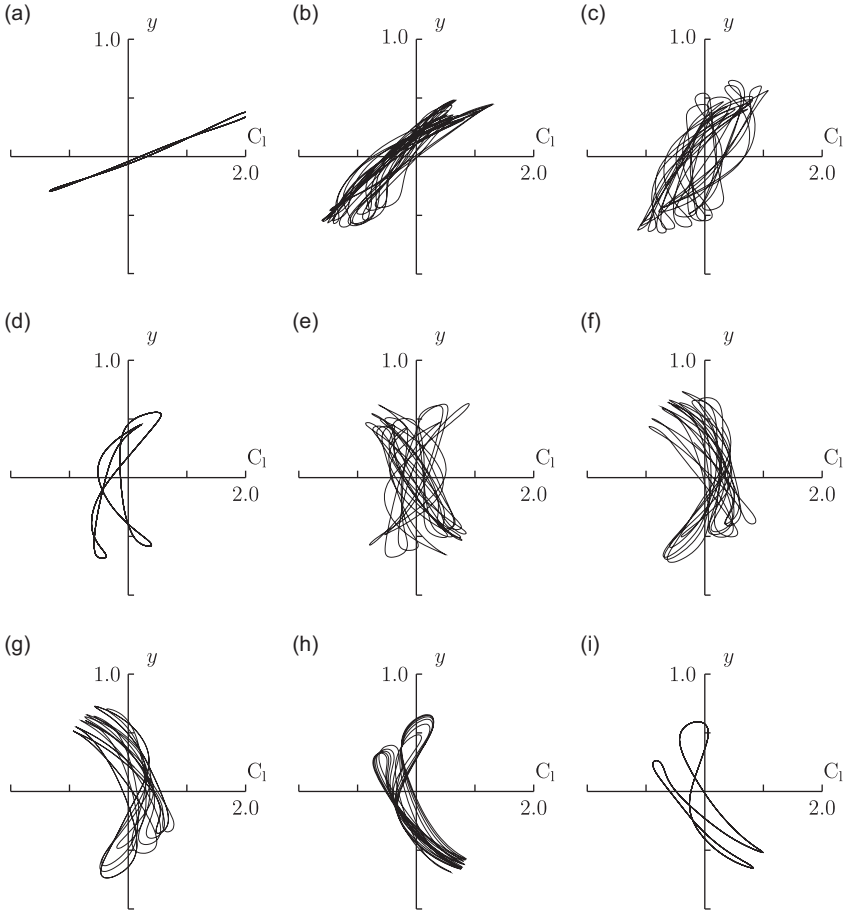

Fig. 6. Lissajou plots, of the lift force against the body displacement, for the sharp corner $r_c = 0$ case, with increasing U^*. The portion of the time history $670 \leq \tau \leq 707$ has been used. (a) $U^* = 2.8$; (b) $U^* = 3.5$; (c) $U^* = 4.2$; (d) $U^* = 4.9$; (e) $U^* = 5.7$; (f) $U^* = 6.4$; (g) $U^* = 7.1$; (h) $U^* = 7.8$; (i) $U^* = 8.5$.

Please cite this article as: Leontini, J.S., Thompson, M.C., Vortex-induced vibrations of a diamond cross-section: Sensitivity to corner sharpness. Journal of Fluids and Structures (2013), http://dx.doi.org/10.1016/j.jfluidstructs.2013.01.002

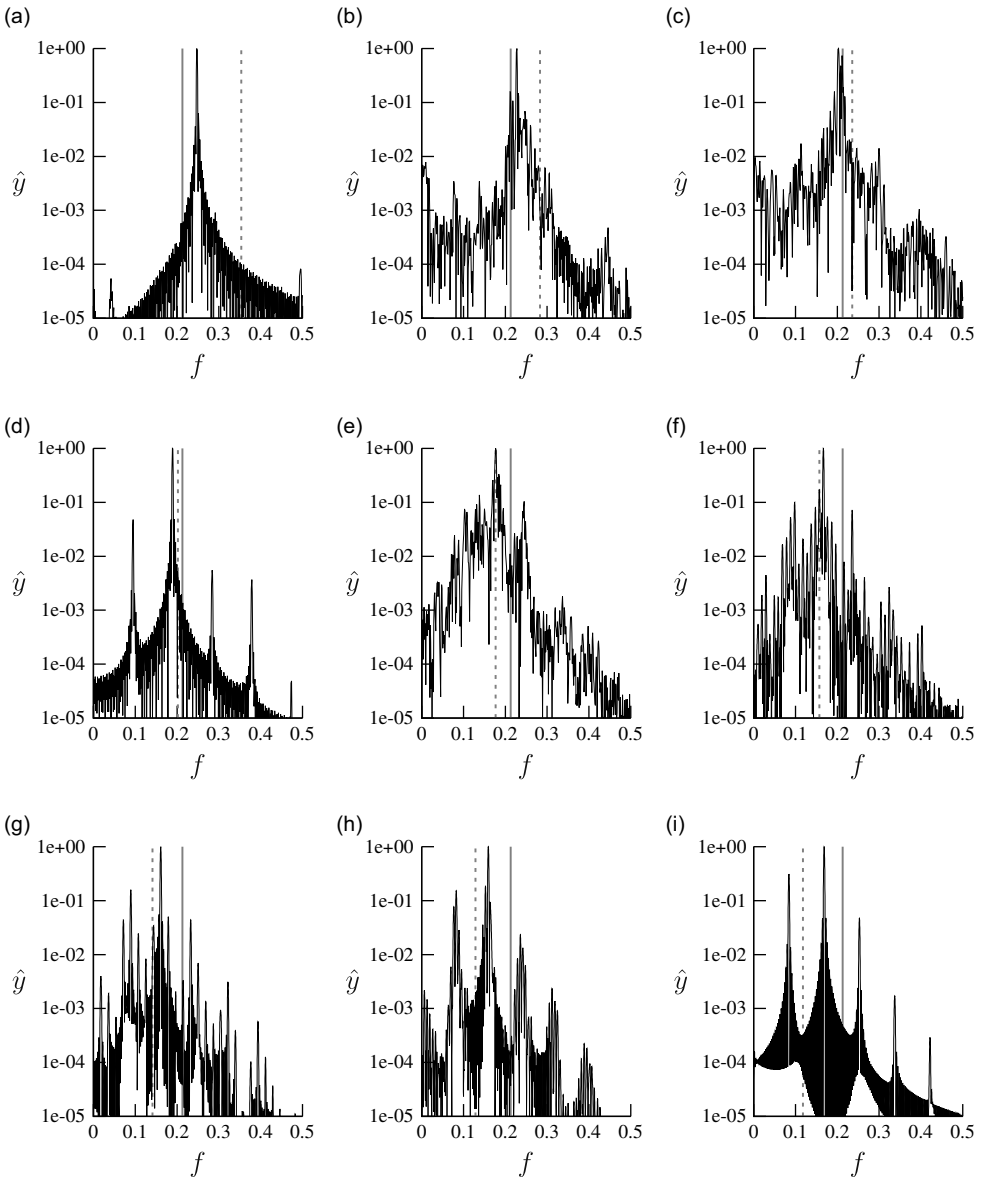

Fig. 7. Spectra of body displacement for the sharp-corner $r_c = 0$ case. (a) $U^* = 2.8$; (b) $U^* = 3.5$; (c) $U^* = 4.2$; (d) $U^* = 4.9$; (e) $U^* = 5.7$; (f) $U^* = 6.4$; (g) $U^* = 7.1$; (h) $U^* = 7.8$; (i) $U^* = 8.5$. The dashed line represents the natural frequency, f_n, the solid horizontal line represents the Strouhal frequency for the rigidly mounted body. Note that these are the same cases as the Lissajou plots presented in Fig. 6.

indicates that the oscillations at this U^* are indeed chaotic. The Lissajou plots show some oscillations similar to the quasiperiodic mode III, and some more similar to the quasiperiodic mode IV (outlined below). Therefore, it seems that this chaos is generated through mode competition between these two states (in fact due to the asymmetry of both of these modes, this mode competition could be between four modes; mode III biased to either side, and mode IV biased to either side).

At $U^* = 4.9$, an interesting phenomenon arises; the flow apparently reorganizes, and the oscillations once again become periodic. However, the period is around twice as long as the period of the initial periodic regime encountered at $U^* = 2.8$, and appears to be a sort of period-doubled mode of oscillation. This can be confirmed from two measurements. First the Lissajou plot of Fig. 6d shows a closed curve, indicating periodicity, that makes two distinct loops. This indicates that there is a primary frequency of oscillation, at which the body oscillates up and down, however two of these up-and-down oscillations need to be conducted before the process repeats exactly. Second, the spectrum of Fig. 7 shows a primary frequency similar to that of the initial periodic regime, corresponding to the frequency of one up-and-down oscillation, with a significant second component at half of the primary frequency, corresponding to the frequency of repetition. This mode, designated mode V, reappears for $U^* > 7.8$.

Please cite this article as: Leontini, J.S., Thompson, M.C., Vortex-induced vibrations of a diamond cross-section: Sensitivity to corner sharpness. Journal of Fluids and Structures (2013), http://dx.doi.org/10.1016/j.jfluidstructs.2013.01.002

This organization is only maintained over a very small range of U^*, as simulations at $U^* = 4.8$ and $U^* = 5.2$ both result in chaotic oscillations. The example at $U^* = 5.7$ clearly shows the return to a chaotic state, and an irregular trajectory being traced in the Lissajou plot of Fig. 6e. The spectrum of Fig. 7e also shows a broadband signature. This appears to be the same mode competition as encountered at $U^* = 4.2$.

Further increases in U^* see the flow gradually become more ordered. Focusing first on the Lissajou plots, as U^* progresses from $U^* = 6.4$, to $U^* = 7.1$, to $U^* = 7.8$ (Fig. 6f–h), the area covered by the trace appears to reduce, with subsequent loops almost retracing the path of the previous loop. The spectra of Fig. 7f–h also reflect this, becoming more "spiky" than broadband, indicating that the flow is closer to quasiperiodic than chaotic. These oscillations are quasiperiodic, based around the subharmonic mode V. Therefore, these quasiperiodic oscillations have been designated mode IV.

For $U^* > 7.9$, the flow synchronizes to a new, subharmonic, periodic state, mode V. This is clear in the Lissajou plot of Fig. 6i, which again shows a closed, double-loop curve. Again, this double-loop curve is indicative of a period-doubled state, and the significant energy at half of the primary frequency of oscillation shown in the spectrum of Fig. 7i confirms this. As previously mentioned, this mode V is the same as that found at $U^* = 4.9$, even though the two are separated by a region of mode competition and quasiperiodicity. One explanation for this is that the stability boundary for mode V is a complicated shape in the parameter space consisting of U^*, Re, and m^*. The flow may also be bistable, and dependent on initial conditions. Further investigation is required to completely understand this phenomenon.

Finally, increasing U^* beyond $U^* = 12.7$ sees the flow return to a classic vortex street, and again oscillate at a frequency close to the Strouhal frequency for a rigid body. In this sense, the oscillations are similar to mode I. However, the oscillation amplitude is significantly higher than mode I, and there is a difference in the timing of vortex shedding. Hence, these oscillations are designated mode VI.

3.4. Flow regimes as a function of U^* and corner radius

The flow regimes identified for the sharp corner case in Section 3.3 are applicable to all of the geometries tested. A map, outlining these flow regimes in the U^*,r_c plane is presented in Fig. 8. These regimes have been delineated based on temporal behaviour, and vortex shedding pattern and timing relative to the body motion.

There are some features of Fig. 8 that are easy to describe. The onset of significant oscillations with increasing U^* appears to be relatively insensitive to the corner radius, occurring around $U^* = 2.8$. For small corner radii, this occurs with a transition to mode II; for the large corner radii, this occurs with a transition to mode VII. These two modes are very similar physically, the only difference being a slight asymmetry in mode II, resulting in a non-zero mean body displacement.

For large values of U^*, the flow settles to mode VI, regardless of corner radius. The value of U^* at the onset of mode VI is however an inverse function of r_c. For small values of r_c, the transition to mode VI is from mode V, whereas for large r_c, the transition to mode VI is from mode VII.

Beyond these features, the picture is far more complex, and the boundaries on the map of Fig. 8 are not as definitive, and therefore have been marked with dashed lines. The two quasiperiodic modes, mode III and mode IV, appear to have very complex stability boundaries. These two modes, as well as large regions of chaotic flow appear to jointly occupy the same region of the map. It is possible that the flow is bistable at many of these values, or that small "tongues" of periodic, quasiperiodic and chaotic response are interleaved throughout this region.

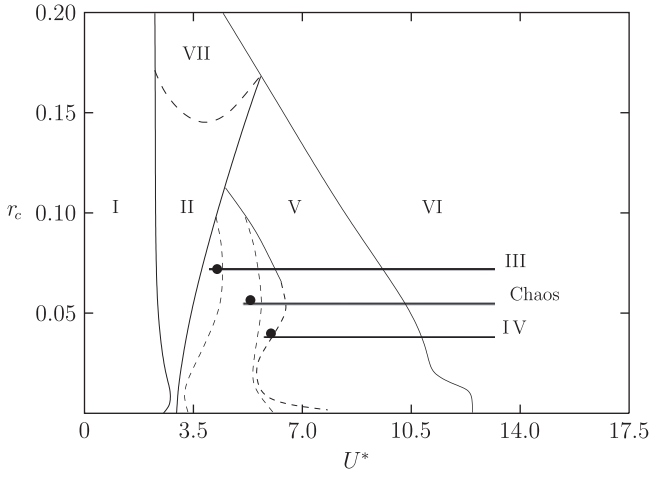

Fig. 8. A map of the flow states encountered as a function of corner radius r_c and U^*. Simulations were run at $r_c = 0$, 0.01, 0.02, 0.05, 0.10, 0.15, 0.20, and steps of $U^* = 0.14$. The various wake states are designated by roman numerals. Definitive borders are marked with solid lines(—); dashed lines (- - -) mark boundaries that are not definitive, due to bi-stability or mode competition.

Please cite this article as: Leontini, J.S., Thompson, M.C., Vortex-induced vibrations of a diamond cross-section: Sensitivity to corner sharpness. Journal of Fluids and Structures (2013), http://dx.doi.org/10.1016/j.jfluidstructs.2013.01.002

The mechanisms leading to chaos also appear to be quite complex. For the sharp corner case, for values of U^* around $U^* = 4.2$, the flow appears to become chaotic via intermittency, whereas for $U^* \geq 5.1$, there seems to be some mode competition between mode III and mode IV. At higher corner radii, the flow seems to switch between the two possible solutions of mode V; one with a positive mean lift, one with a negative mean lift.

3.5. Vortex shedding patterns for each of the flow regimes

Each of the flow states mapped in Fig. 8 presents a unique vortex shedding pattern. The wide range of possible states, particularly for the sharp corner cases, is a result of the interaction of vortices being shed from the sharp corner (essentially a leading edge) and the sharp trailing edge of the body. Images of vorticity for each state, along with identification of the salient features of the vortex formation and shedding process, are presented in the following sections.

3.5.1. Mode I

Mode I consists of relatively small oscillations, however these oscillations can be chaotic, regardless of corner radius. This chaotic fluctuation does not disappear until synchronization to the periodic, but asymmetric, mode II, or the periodic mode VI. It is hypothesized that these fluctuations are a direct consequence of the sharp trailing edge of the body, which leads to a complex interaction between the forming vortices being shed from the side corners of the body, and smaller vortices formed in the recirculation regions along each of the rear edges. Evidence for this interaction can be found in the animations of the flow found in the online supplemental material (Video 1 and Video 2). It is the interaction of these vortex systems that results in chaos (Fig. 9).

Supplementary material related to this article can be found online at doi: http://dx.doi.org/10.1016/j.jfluidstructs.2013.01.002.

3.5.2. Mode II

Mode II consists of a mode that oscillates periodically at a frequency close to the natural structural frequency. This mode is asymmetric, with a non-zero mean body displacement, and non-zero mean lift. This asymmetry is reflected in the vortex shedding, yet the exact configuration of vortices in the wake depends on the values of U^* and r_c.

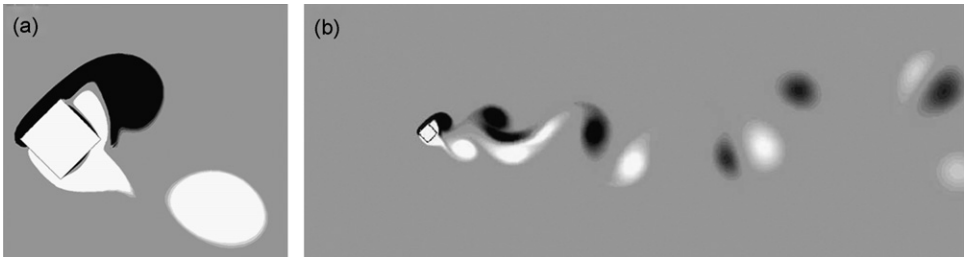

Fig. 9. An example of the flow for mode I. Instantaneous snapshots of vorticity at $\tau = 415.78$ of the flow (a) close to the body and (b) of the far wake for $r_c = 0$, $U^* = 2.12$. The vortex formation and shedding process is complicated by the presence of the sharp corners.

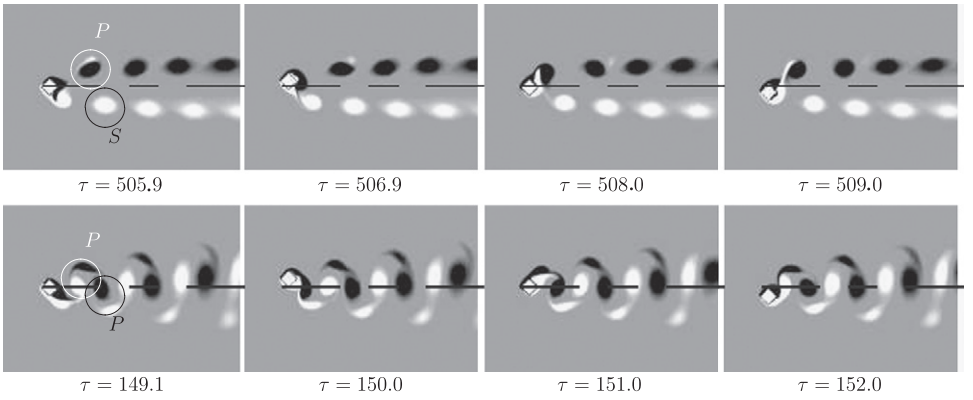

Fig. 10. A series of images of vorticity of mode II. The images show progressions in time, reading left to right, for two cases (the time instant of each image is stated below the image). The top row is for $r_c = 0$, $U^* = 2.8$, the bottom row is for $r_c = 0.1$, $U^* = 3.5$. The sequence of images progress from displacement close to zero, maximum displacement, displacement close to zero, minimum displacement. Both examples have a non-zero mean lift, but different configurations of vortices in the wake. The relevant pairs and single vortices are annotated with a P and S, respectively, and marked with black and white circles, in the first image of each sequence. The top example shows a weak P+S wake (the pair consisting of a strong negative (black) vortex and a much weaker weak positive (white) vortex). The bottom example shows a 2P vortex configuration, with pairs consisting of almost equal strength positive and negative vortices.

Please cite this article as: Leontini, J.S., Thompson, M.C., Vortex-induced vibrations of a diamond cross-section: Sensitivity to corner sharpness. Journal of Fluids and Structures (2013), http://dx.doi.org/10.1016/j.jfluidstructs.2013.01.002

Fig. 10 shows two examples of mode II. In the first, for $r_c = 0.0$ and $U^* = 2.8$, the asymmetry manifests as a P+S mode, albeit one where the second vortex in the pair is very much weaker than the first. In the second, for $r_c = 0.1$ and $U^* = 3.5$, the flow is an asymmetric 2P mode, where the pair on one side is stronger than the other.

The vortex formation is influenced by the interaction between the separating shear layer and the sharp trailing edge. For the case that develops into the P+S mode, the forming vortex on one side is augmented by the sweep of the sharp trailing edge across the wake. This sweep forms a trailing edge vortex, on the opposite side of the wake to the leading edge vortex of the same sign. The trailing edge vortex pairs with the forming vortex of opposite sign, while the leading edge vortex is shed alone to form the single vortex. For the 2P mode, both forming vortices are chopped by the trailing edge. This process is illustrated in the animations provided in the online supplementary material (Video 3 and Video 4), for the same case as Fig. 10.

Supplementary material related to this article can be found online at doi: http://dx.doi.org/10.1016/j.jfluidstructs.2013.01.002.

This interaction between leading and trailing edge is critical to the formation of this mode. For the cases where the leading "edge" is essentially removed (by making the top and bottom corners more rounded), this asymmetric mode disappears. It also seems that the sharp trailing edge has a very important role to play, and these asymmetric modes may disappear if the trailing edge is rounded. This fits with the observation of Sheard et al. (2009), that asymmetry occurred in the wake of a rigid sharp corner diamond, but was eliminated by rounding the trailing edge.

3.5.3. Mode III

With the onset of mode III, mode II loses its periodicity, becoming quasiperiodic. This quasiperiodicity is generated physically not by a significant change in the vortex shedding process, but by some complicated vortex pairing and merging in the wake at around 8D downstream. This pairing and merging causes a modulation of the lift force on the body, and therefore causes an amplitude modulation of the body displacement.

Fig. 11 shows this process in a series of images. The amplitude modulation period is around 3–3.5 times the oscillation period. The sequence of images covers three oscillation periods, showing images taken at the maximum body displacement in each direction. A portion of the time history of the body displacement is shown at the top of the image, showing the amplitude modulation, and the time of each image is marked with a dot and the dotted line. The images show

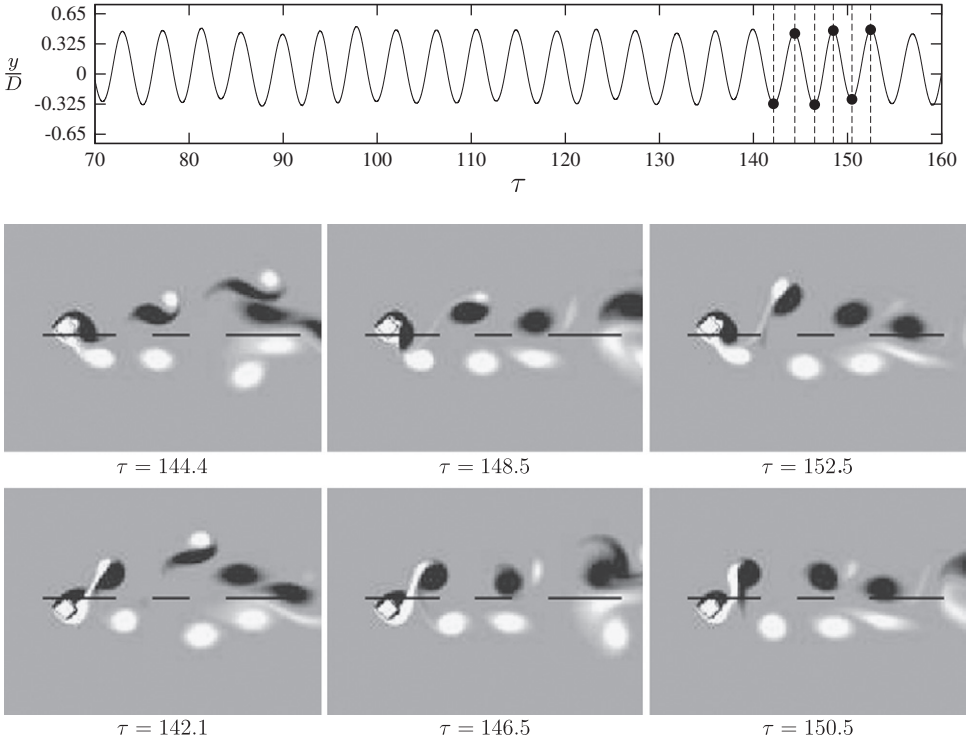

Fig. 11. A series of images of vorticity showing the structure of mode III, for $U^* = 3.1$ and $r_c = 0$. The images progress in time from bottom to top, left to right. The bottom row of images show the wake when the body is at maximum negative displacement, the top row show the wake when the body is a maximum positive displacement. The images are half a period apart, and cover three consecutive oscillations. The time of each image is marked with the black circle (•) and the dotted line in the time history at the top of the figure. The images show that the vortex formation and shedding immediately behind the body is similar in each oscillation, yet there is complex vortex pairing and merging occurring approximately 8D downstream, leading to amplitude modulation of the body displacement.

Please cite this article as: Leontini, J.S., Thompson, M.C., Vortex-induced vibrations of a diamond cross-section: Sensitivity to corner sharpness. Journal of Fluids and Structures (2013), http://dx.doi.org/10.1016/j.jfluidstructs.2013.01.002

that the wake is essentially in a P+S mode, and that in the near wake, the vortex formation and shedding process is quite similar in each consecutive oscillation. However, small changes in the timing of the vortex formation and shedding relative to the body oscillation leads to complicated vortex dynamics further downstream. In all the images, the organized structure of the pure P+S wake quickly breaks down, and the shed vortices pair and merge in a complicated manner approximately 8D downstream. Animations of the shedding process close to the body, and of the wake further downstream, are providing for the same case as Fig. 11 in the online supplementary material (Video 5 and Video 6).

Supplementary material related to this article can be found online at doi: http://dx.doi.org/10.1016/j.jfluidstructs.2013.01.002.

As U^* is increased further beyond the loss of stability of the original mode II, the pairing and merging becomes more complicated, and the wake rapidly becomes chaotic.

3.5.4. Mode IV

Mode IV is a quasiperiodic mode, with a slow growth and decay of the oscillations over a long time. The basic oscillations are very similar to those of mode V (described in Section 3.5.5), except for this long period modulation.

Fig. 12 shows a portion of the time history for an example of mode IV, for the sharp corner case $r_c = 0$ at $U^* = 7.8$. Animations of this case are provided in the online supplementary material (Video 7 and Video 8). Approximately two long periods are shown. The time history shows that the basic oscillations consist of a type of period doubled mode, where every "even" oscillation reaches a higher maximum displacement than the previous "odd" oscillation. However, there is an amplitude modulation of this basic oscillation cycle. Over one cycle of this modulation (starting, for example, around $\tau = 590$ in the time history of Fig. 12), the higher "even" maxima decrease, and the lower "odd" maxima increase, until they essentially match (around $\tau = 780$ in the time history of Fig. 12). At this point, the cycle begins again, with a sudden increase in the first "even" maximum of the next cycle.

Supplementary material related to this article can be found online at doi: http://dx.doi.org/10.1016/j.jfluidstructs.2013.01.002.

This amplitude modulation coincides with a subtle change in the phase of the vortex shedding with respect to the body motion. The images of Fig. 12 show the progression of the wake configuration over a cycle of amplitude modulation.

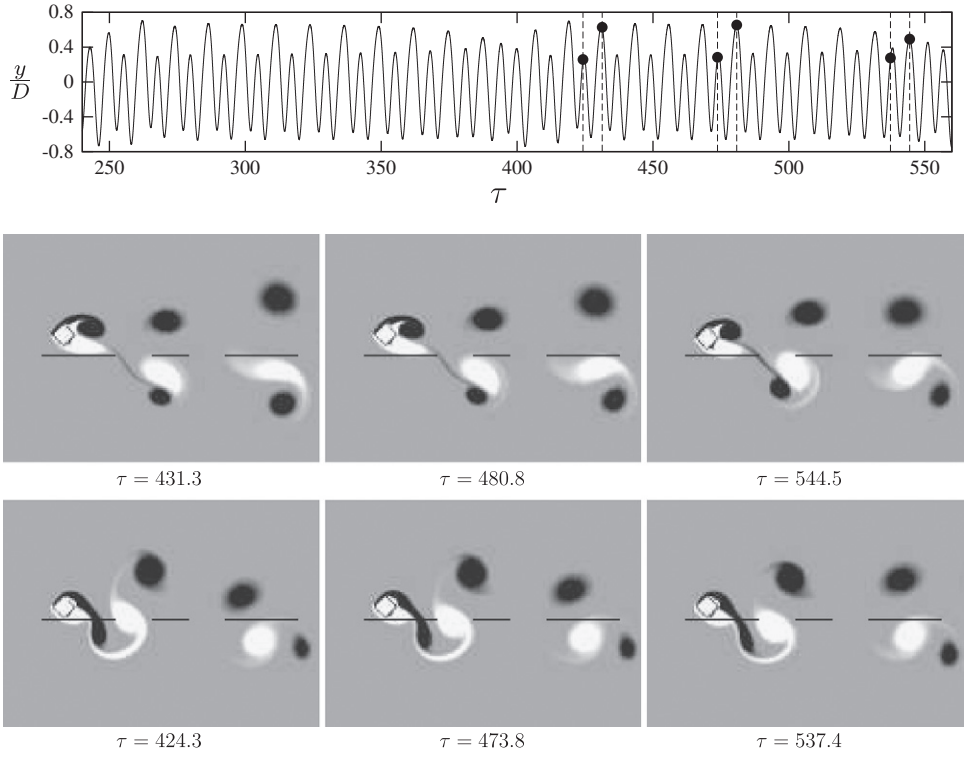

Fig. 12. An example of mode IV, for $U^* = 7.8$ and $r_c = 0$. Time history of the body displacement, showing approximately two long cycles of the quasiperiodic oscillation, and a series of images of vorticity showing the development of the wake over this cycle. The instant of each of the images is marked on the time history with a black dot and dotted vertical line. The time history shows, in general, every "even" oscillation reaches a higher maximum than the previous "odd" oscillation. Over a quasiperiodic cycle, the "even" maxima decrease, and the "odd" maxima increase, until they match, and the cycle begins again. Each bottom-top pair of images shows an "odd–even" pair of maxima. The images show that over the quasiperiodic cycle, the flow oscillation is relatively subtle, basically consisting of small changes of phase between the body oscillation and vortex shedding, which results in changes in vortex placement, and therefore wake width.

Please cite this article as: Leontini, J.S., Thompson, M.C., Vortex-induced vibrations of a diamond cross-section: Sensitivity to corner sharpness. Journal of Fluids and Structures (2013), http://dx.doi.org/10.1016/j.jfluidstructs.2013.01.002

Each of the images is taken at an instant where the body displacement is close to a local maximum. The top row of images represent "even" cycles, with the higher local maxima, and the bottom row of images represent "odd" cycles, with low local maxima. Each top image is approximately one oscillation cycle forward in time with respect to the corresponding bottom image. The images show that the wake development is not dramatic, with small changes in the timing of vortex shedding resulting in small changes of vortex placement and therefore wake width. However, close to the end of the modulation cycle (represented by the final two images), the "even" and "odd" cycles become harder to distinguish, the similar displacement amplitude resulting in similar wake configurations.

As U^* is decreased from the mode IV to mode V transition (around $U^* = 7.9$), the period of the amplitude modulation is reduced. An indication of this can been seen in the spectra presented in Fig. 7. The spectra representing mode IV (particularly those for $U^* = 7.8$ and $U^* = 7.1$, Fig. 7h and g respectively) show the same primary frequencies ($f = 0.11$ and its harmonics), but secondary frequencies around this gradually moving away with decreasing U^*. The frequency of the amplitude modulation is governed by the difference between the primary frequency and these secondary frequencies. Therefore, as these secondary frequencies move further from the primary, the frequency of the amplitude modulation increases, and the period decreases.

3.5.5. Mode V

Mode V consists of a mode that oscillates periodically, at a frequency close to the natural structural frequency. However, two oscillations are required for the flow to repeat, and so this mode is period doubled.

Fig. 13, and the animations provided in the online supplementary material (Video 9 and Video 10), shows a series of images taken over one period of repetition. The series of images start at an instant where the body displacement is close to zero, then at a maximum displacement, then again close to zero, then at a minimum displacement. This sequence is repeated twice due to the period doubled nature of the mode. Note that the images are not equi-spaced in time, as the two oscillation cycles that make up one full period are not quite the same length, nor are they completely sinusoidal.

Supplementary material related to this article can be found online at doi: http://dx.doi.org/10.1016/j.jfluidstructs.2013.01.002.

During the upstroke of the first cycle (the top row of Fig. 13) the top shear layer stays attached to the body, all the way to the sharp trailing edge, where it eventually separates. This separated shear layer goes on to form a weak vortex shed from the trailing edge, that is paired with the forming vortex from the bottom shear layer, that is essentially shed from the sharp corner leading edge. This process is illustrated in the first two images of Fig. 13. During the downstroke, the top shear layer separates from the sharp corner leading edge, and rolls up into a vortex that is shed into the wake. This is illustrated in the third and fourth images of Fig. 13.

The vortex formation and shedding process for the second cycle is similar, but subtly shifted in phase compared to the first cycle. The pair is still formed during the upstroke, but the weak vortex, shed from the upper shear layer from the sharp trailing edge of the body, is shed much later, practically when the body has begun its downstroke. This is shown in the fifth, sixth, and seventh images of Fig. 13. This same process seems to weaken the forming leading edge vortex of the upper shear layer that is formed and eventually shed near the end of the downstroke. Comparison of the eighth image with the fourth image of Fig. 13 shows that the shed negative vortex (shed from the top leading edge) is weaker (smaller) in the second cycle compared to the first.

3.5.6. Mode VI

The final identified mode for the sharp corner case, mode VI, occurs for relatively high values of U^*, typically $U^* > 12.7$. This mode is periodic, and particularly for the sharp corner cases, still results in a significant oscillation amplitude.

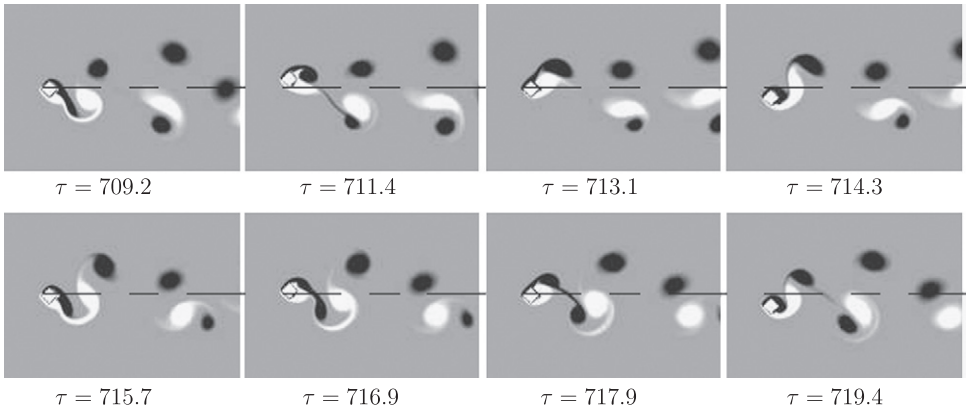

Fig. 13. A series of images of vorticity of mode V, for $U^* = 8.5$ and $r_c = 0$. Images show the progression in time, reading left to right, top to bottom. The sequence of images progress from displacement close to zero, maximum displacement, displacement close to zero, minimum displacement, repeated twice. Comparing the top row to the bottom row shows the difference between two subsequent oscillations. The wake configuration is a P+S mode, but essentially period doubled.

Please cite this article as: Leontini, J.S., Thompson, M.C., Vortex-induced vibrations of a diamond cross-section: Sensitivity to corner sharpness. Journal of Fluids and Structures (2013), http://dx.doi.org/10.1016/j.jfluidstructs.2013.01.002

Fig. 14 shows a series of images of mode VI, separated in time by a quarter of an oscillation cycle. This mode oscillates at a frequency close to the Strouhal frequency for a fixed body, similar to mode II and mode VII. However, unlike mode II, this mode is spatio-temporally symmetric, similar to the classic Kármán vortex street. Also, comparing Fig. 14 with Fig. 15 (both of which show the body at approximately the same four points in the oscillation cycle, for mode VI and mode VII respectively) shows that there is a change in the phase between the body oscillation and the vortex shedding. Further confirmation of this behaviour is found in the animations of the case of Fig. 14 provided in the online supplementary material (Video 11 and Video 12). This is similar to the behaviour for a circular cylinder, which sees the phase ϕ between the body motion and the lift force (which is heavily influenced by the vortex shedding) jump from close to 0° to around 180° in experiments (Govardhan and Williamson, 2000), or slide between these same two limits in lower Re simulations (Leontini et al., 2006b).

Supplementary material related to this article can be found online at doi: http://dx.doi.org/10.1016/j.jfluidstructs.2013.01.002.

Fig. 16 shows the phase between the body displacement and the lift force, for the body with the most rounded corners, $r_c = 0.2$. This phase was obtained by finding the maximum of the cross-correlation between the two signals. This figure shows that, like the experiments using circular cylinders, there is a distinct jump in the phase from close to 0° to around 180°. In fact, it is this change in phase that delineates mode VI from mode VII, as the two have the same spatio-temporal symmetries and basic organization of vortices in the wake.

3.5.7. Mode VII

The last clearly identifiable mode is mode VII. This mode occurs only for the well-rounded corner bodies. The wake configuration of this mode is the classic Kármán vortex street, or the 2S mode. The frequency of oscillation is similar to the

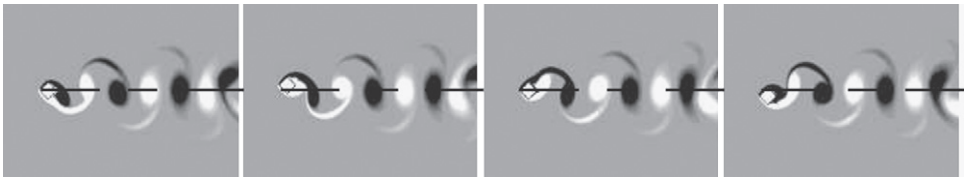

Fig. 14. A series of images of vorticity of mode VI, for $U^* = 14.1$ and $r_c = 0$. Images show the progression in time, reading left to right, top to bottom. The sequence of images progress from displacement close to zero, maximum displacement, displacement close to zero, minimum displacement.

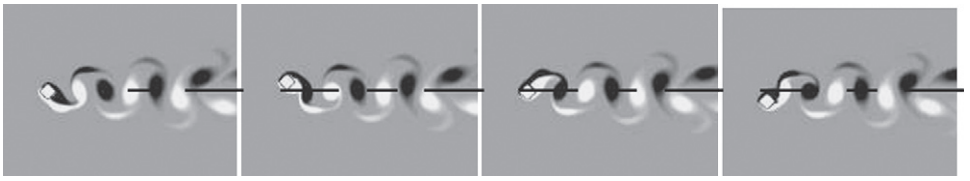

Fig. 15. A series of images of vorticity of mode VII, for $U^* = 3.5$ and $r_c = 0.2$. Images show the progression in time, reading left to right, top to bottom. The sequence of images progress from displacement close to zero, maximum displacement, displacement close to zero, minimum displacement.

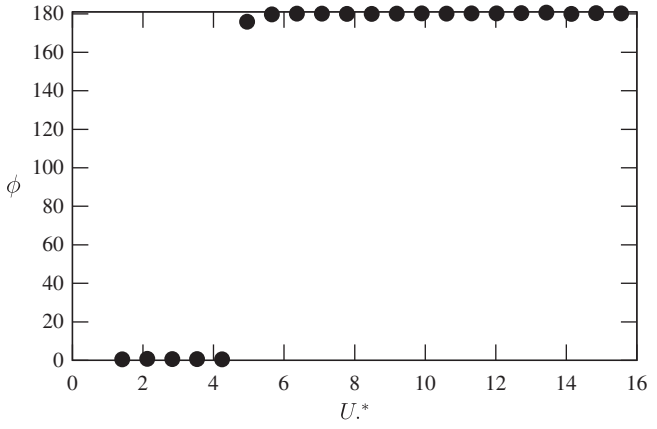

Fig. 16. Phase between the body displacement and lift force, for $r_c = 0.2$, as a function of U^*. The sudden jump from 0° to 180° delineates mode VI from mode VII.

Please cite this article as: Leontini, J.S., Thompson, M.C., Vortex-induced vibrations of a diamond cross-section: Sensitivity to corner sharpness. Journal of Fluids and Structures (2013), http://dx.doi.org/10.1016/j.jfluidstructs.2013.01.002

natural structural frequency. This mode is similar in behaviour to the asymmetric mode II, apart from the fact that it maintains the spatio-temporal symmetry of the Kármán vortex street. Again, animations of the case outlined in Fig. 15 are also provided in the online supplementary material (Video 13 and Video 14).

Supplementary material related to this article can be found online at doi: http://dx.doi.org/10.1016/j.jfluidstructs.2013.01.002.

3.6. Further discussion of mode competition leading to chaos

Chaos through mode competition or mode interaction occurs in a variety of fluid-mechanical systems (Crawford and Knobloch, 1991). The work of Ciliberto and Gollub (1984) showed mode competition between stationary wave patterns in the Faraday experiment (where a layer of fluid with a free surface is oscillated vertically at a set amplitude and frequency) could lead to either slowly varying-amplitude oscillations or more complex chaotic oscillations. Their heuristic model was able to produce many of the features of the full system.

In a system where the patterns are not stationary, but periodic, the addition of a slowly varying amplitude essentially renders the flow quasiperiodic. Therefore, it may be expected that mode competition will lead to quasiperiodicity and chaos in the wake of an elastically mounted bluff body. This is in fact observed for the elastically mounted diamond studied here.

The study of Crawford and Knobloch (1991) explains that, from a theoretical point of view, mode interactions arise when there are two separate solutions which bifurcate from a given base state. Ciliberto and Gollub (1984) showed that, in a practical sense, this means mode competition is likely to arise in regions of the parameter space that separate regions dominated by different modes. The chaotic region shown in Fig. 8, between mode III and mode IV (themselves quasiperiodic "versions" of the periodic mode II and mode V), is such a region.

Further qualitative evidence of mode competition between mode II and mode V leading to chaos is presented in Fig. 17, which shows the time history of oscillation and six snapshots of vorticity for a case in the chaotic region of parameter space, $U^* = 5.7$ and $r_c = 0$. The time history shows that the oscillation is modulated in an irregular way, while the snapshots show that at times the wake resembles the wake of mode II (shown in Fig. 10), and at other times resemble the wake of mode V (shown in Fig. 13). The flow essentially oscillates irregularly between these two patterns. While not unequivocal, the results indicate the presence of mode competition.

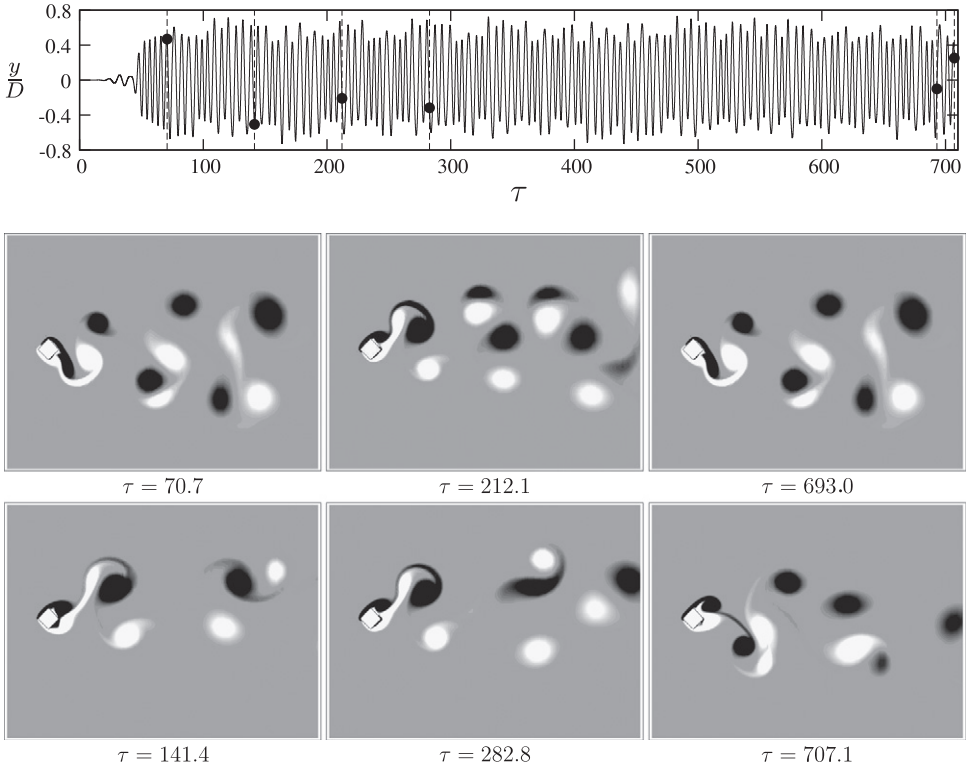

Fig. 17. Qualitative evidence for chaos driven by mode competition, for $U^* = 5.7$ and $r_c = 0$. Time history of the body displacement, and a series of images of vorticity showing the changes in wake vortex organization over time. The instant of each of the images is marked on the time history with a black dot and dotted vertical line. The images are organized such that the progression in time is from top to bottom, left to right. The top row of images show instants where the near wake is similar in structure to the periodic mode II; the bottom row show instants where the near wake is more similar to the periodic but subharmonic mode V. The images show that the flow essentially oscillates irregularly between these two patterns.

Please cite this article as: Leontini, J.S., Thompson, M.C., Vortex-induced vibrations of a diamond cross-section: Sensitivity to corner sharpness. Journal of Fluids and Structures (2013), http://dx.doi.org/10.1016/j.jfluidstructs.2013.01.002

4. Concluding remarks

A systematic parameter study of diamond cross-sections undergoing VIV has been performed, specifically investigating the impact of the sharpness of the side corners. These results have been compared with those for the canonical bluff body, the circular cylinder.

For rigid (non-oscillating) bodies, it has been shown that the lift and drag forces are strong functions of the sharpness of these corners. However, the configuration of the wake is essentially the same in all cases, and is the classic Kármán vortex street. However, for the elastically mounted bodies, it has been shown that, particularly for sharp corner bodies, the flow response is markedly more varied than for the circular cylinder. At least six different flow regimes, as a function of U^*, can be identified, many with distinct symmetry properties. Of particular interest is the disappearance of a high-amplitude regime that is synchronized to a frequency near the natural structural frequency, and the appearance of a chaotic regime, with higher peak amplitudes than those achieved from a circular cylinder, that exists over a significantly wide band of U^*, for corner radii $r_c \leq 0.10$.

As the side corners are progressively rounded, the flow response moves from "diamond-like" to "cylinder-like", as the number of flow regimes possible as a function of U^* decreases. For corner radii $r_c > 0.15$, the response types are similar to those encountered for a circular cylinder.

Acknowledgements

The authors would like to acknowledge the help of Mr. G.C. Lim in the running of the preliminary simulations for this study. This work was financially supported under Grant no. DP110102141 as part of the Discovery Grants program of the Australian Research Council.

Appendix A. Supplementary material

Supplementary data associated with this paper can be found in the online version, at http://dx.doi.org/10.1016/j.jfluidstructs.2013.01.002.

References

Ajith Kumar, R., Sohn, C., Lakshmana Gowda, B., 2009. Influence of corner radius on the near wake structure of a transversely oscillating square cylinder. Journal of Mechanical Science and Technology 23, 2390–2416.

Bearman, P., Gartshore, I., Maull, D., Parkinson, G., 1987. Experiments on flow-induced vibration of a square-section cylinder. Journal of Fluids and Structures 1, 19–34.

Bearman, P.W., 1984. Vortex shedding from oscillating bluff bodies. Annual Review of Fluid Mechanics 16, 195–222.

Blackburn, H.M., Henderson, R., 1996. Lock-in behaviour in simulated vortex-induced vibration. Experimental Thermal and Fluid Science 12, 184–189.

Bokaian, A., Geoola, F., 1984. Hydroelastic instabilities of square cylinders. Journal of Sound and Vibration 92, 117–141.

Bourguet, R., Karniadakis, G.Em, Triantafyllou, M., Multi-frequency vortex-induced vibrations of a long tensioned beam in linear and exponential shear flows. Journal of Fluids and Structures, http://dx.doi.org/10.1016/j.jfluidstructs.2012.07.007, in press.

Ciliberto, S., Gollub, J., 1984. Pattern competition leads to chaos. Physical Review Letters 52, 922–926.

Corless, R., Parkinson, G., 1988. A model of the combined effects of vortex-induced oscillation and galloping. Journal of Fluids and Structures 2, 203–220.

Corless, R., Parkinson, G., 1993. Mathematical modelling of the combined effects of vortex-induced vibration and galloping. Part II. Journal of Fluids and Structures 7, 825–848.

Crawford, J., Knobloch, E., 1991. Symmetry and symmetry-breaking bifurcations in fluid dynamics. Annual Review of Fluid Mechanics 23, 341–387.

Dalton, C., 2003. Numerical solutions of a viscous uniform approach flow past square and diamond cylinders. Journal of Fluids and Structures 18, 455-465.

Deniz, S., Staubli, T., 1997. Oscillating rectangular and octagonal profiles: interaction of leading- and trailing-edge vortex formation. Journal of Fluids and Structures 11, 3–31.

Govardhan, R., Williamson, C.H.K., 2000. Modes of vortex formation and frequency response of a freely vibrating cylinder. Journal of Fluid Mechanics 420, 85–130.

Govardhan, R., Williamson, C.H.K., 2002. Resonance forever: existence of a critical mass and an infinite regime of resonance in vortex-induced vibration. Journal of Fluid Mechanics 473, 147–166.

Hartlen, R., Currie, I., 1970. Lift-oscillator model for vortex-induced vibrations. Journal of Engineering Mechanics (American Society of Civil Engineers) 96, 577–591.

Hover, F.S., Techet, A.H., Triantafyllou, M.S., 1998. Forces on oscillating uniform and tapered cylinders in crossflow. Journal of Fluid Mechanics 363, 97–114.

Karniadakis, G., Sherwin, S., 2005. Spectral/hp Element Methods for Computational Fluid Dynamics, 2nd edition, Oxford University.

Khalak, A., Williamson, C.H.K., 1999. Motions, forces and mode transitions in vortex-induced vibrations at low mass–damping. Journal of Fluids and Structures 13, 813–851.

Korkischko, I., Meneghini, J., 2012. Suppression of vortex-induced vibration using moving surface boundary-layer control. Journal of Fluids and Structures 34, 259–270.

Lee, H.B., Lee, T.R., Chang, Y.S., 2013. Numerical simulation of flow-induced bi-directional oscillations. Journal of Fluids and Structures Structures 37, 220–231.

Leontini, J., Lo Jacono, D., Thompson, M., 2011. A numerical study of an inline oscillating cylinder in a free stream. Journal of Fluid Mechanics 688, 551–568.

Leontini, J., Thompson, M., Hourigan, K., 2006a. The beginning of branching behaviour of vortex-induced vibration during two-dimensional flow. Journal of Fluids and Structures 22, 857–864.

Leontini, J., Thompson, M., Hourigan, K., 2007. Three-dimensional transition in the wake of a transversely oscillating cylinder. Journal of Fluid Mechanics 577, 79–104.

Please cite this article as: Leontini, J.S., Thompson, M.C., Vortex-induced vibrations of a diamond cross-section: Sensitivity to corner sharpness. Journal of Fluids and Structures (2013), http://dx.doi.org/10.1016/j.jfluidstructs.2013.01.002

Leontini, J.S., Stewart, B.E., Thompson, M.C., Hourigan, K., 2006b. Wake-state and energy transitions of an oscillating cylinder at low Reynolds number. Physics of Fluids 18, 067101.

Lo Jacono, D., Leontini, J., Thompson, M., Sheridan, J., 2010. Modification of three-dimensional transition in the wake of a rotationally oscillating cylinder. Journal of Fluid Mechanics 643, 349–362.

Morse, T., Williamson, C., 2010. Steady, unsteady and transient vortex-induced vibration predicted using controlled motion data. Journal of Fluid Mechanics 649, 429–451.

Nemes, A., Zhao, J., Lo Jacono, D., Sheridan, J., 2012. The interaction between flow-induced vibration mechanisms of a square cylinder with varying angles of attack. Journal of Fluid Mechanics 710, 102–130.

Parkinson, G., Smith, J., 1964. The square prism as an aeroelastic non-linear oscillator. Quarterly Journal of Mechanics and Applied Mathematics XVII, 225–239.

Ryan, K., Thompson, M., Hourigan, K., 2005. Variation in the critical mass ratio of a freely oscillating cylinder as a function of Reynolds number. Physics of Fluids 17, 038106.

Sánchez-Sanz, M., Velazquez, A., 2009. Vortex-induced vibration of a prism in internal flow. Journal of Fluid Mechanics 641, 431–440.

Sarpkaya, T., 2004. A critical review of the intrinsic nature of vortex-induced vibrations. Journal of Fluids and Structures 19, 389–447.

Sheard, G., Fitzgerald, M., Ryan, K., 2009. Cylinders with square cross-section: wake instabilities with incidence angle variation. Journal of Fluid Mechanics 630, 43–69.

Singh, S., Mittal, S., 2005. Vortex-induced oscillations at low Reynolds numbers: hysteresis and vortex-shedding modes. Journal of Fluids and Structures 20, 1085–1104.

Staubli, T., 1983. Calculation of the vibration of an elastically mounted cylinder using experimental data from forced oscillation. Journal of Fluids Engineering 105, 225–229.

Tamura, T., Miyagi, T., Kitagishi, T., 1998. Numerical prediction of unsteady pressures on a square cylinder with various corner shapes. Journal of Wind Engineering and Industrial Aerodynamics 74–76, 531–542.

Thompson, M.C., Hourigan, K., Sheridan, J., 1996. Three-dimensional instabilities in the wake of a circular cylinder. Experimental Thermal and Fluid Science 12, 190–196.

Williamson, C.H.K., Govardhan, R., 2004. Vortex-induced vibrations. Annual Review of Fluid Mechanics 36, 413–455.

Williamson, C.H.K., Roshko, A., 1988. Vortex formation in the wake of an oscillating cylinder. Journal of Fluids and Structures 2, 355–381.

Zhao, J., Nemes, A., Lo Jacono, D., Sheridan, J., 2010. The effect of incidence angle variation of a square cylinder on its dynamic response and wake states. In: Proceedings of the 17th Australasian Fluid Mechanics Conference.

Please cite this article as: Leontini, J.S., Thompson, M.C., Vortex-induced vibrations of a diamond cross-section: Sensitivity to corner sharpness. Journal of Fluids and Structures (2013), http://dx.doi.org/10.1016/j.jfluidstructs.2013.01.002